Skin friction and surface optical flow in viscous flows

Tianshu Liu[1a], Tao Chen[2], David M. Salazar[1], Massimo Miozzi[3]

1. Department of Mechanical and Aerospace Engineering

Western Michigan University, Kalamazoo, MI 49008, USA

2. Department of Mechanics and Aerospace Engineering

Southern University of Science and Technology, Shenzhen, China

3. CNR-INM, Marine Technology Institute of National Research Council, Rome, Italy

(Revision for Physics of Fluids for consideration as a research paper)

(05/11/2022)

a: The corresponding author

Department of Mechanical and Aerospace Engineering, Western Michigan University,

Kalamazoo, MI, USA. tianshu.liu@wmich.edu, 269-276-3426

Abstract

The relationship between skin friction and the surface optical flow (SOF) in viscous flows is discussed based on the evolution equations of surface temperature, scalar and enstrophy where the SOF is defined as the convection velocity of these quantities. Physically, the SOF is proportional to skin friction, which can be determined by solving the optical flow equation re-cast from these evolution equations. This optical flow method can be applied to surface temperature and mass transfer visualizations to extract skin friction fields in experiments. To examine this method, it is first applied to complex surface enstrophy structures obtained in direct numerical simulation (DNS) data of a turbulent channel flow. Further, it is applied to surface temperature structures obtained in time-resolved temperature sensitive paint (TSP) measurements in a flow over a National Advisory Committee for Aeronautics (NACA) 0015 airfoil model and an impinging jet.

1. Introduction

Skin friction is the wall shear stress that is a major contributor to the fluid-mechanic drag. Skin friction vector fields reveal the complex flow topology particularly in three-dimensional (3D) separated flows and turbulent boundary layers [1-6]. In particular, near-wall flow structures in separated flows and turbulent flows are determined by the skin friction field and the surface pressure field [7-11]. Global skin friction diagnostics give high-resolution skin friction fields extracted from certain measurable quantities in conventional surface flow visualizations in experimental fluid mechanics, including surface oil film, heat transfer, mass

transfer, and pressure visualizations [12, 13]. To extract skin friction from these quantities is an inverse problem. Relations between skin friction and measured quantities are derived by projecting the relevant governing equations for surface flow visualizations onto the image plane [14].

The analysis for extraction of normalized skin friction vector fields from surface temperature maps is based on a relation obtained from the asymptotic expansion of the energy equation at the wall [15, 16]. A time sequence of skin friction vector fields with high spatial and temporal resolution is obtained via a variational method as the solution of an ill-posed problem. However, this method has several unknown parameter in the problem formulation heading towards an unknown forcing term and a normalized solution. Moreover, the input required by the optical flow problem formulation reported in [15, 16] requires a temperature field whose evolution relies uniquely on the colder fluid interaction with the warmer wall through the boundary layer. Practically, this simple condition poses a challenging technological constraint because it requires an almost uniform heat flux between the model and the flow. Roughly speaking, the model heating system has to balance the heat removed by the flow. By supplying a corresponding heat flux in time, the temperature differences within the model body are negligible in respect to the difference between body and external fluid.

Experimental setups placing the heating system in the outer peel of the model satisfies the Biot-number-uniformity requirement because they accommodate the heat flux source very close to the heat flux sink. On the other side, this solution involves non-trivial technological

knowledge and resources. Internal heating systems at a constant distance to the cooled surface also satisfy the Biot-number-uniformity requirement, as the circular cylinder model [16].

To find an alternative, Miozzi et al. [17-20] studied the feasibility of quantitative estimation of skin friction by using the traces of temperature disturbances at the wall, on the basis of the relationship between the celerity of propagation of temperature disturbances and the friction velocity. This relationship grounds on the experimental evidence of a relation of between the time histories of the friction velocity and the celerity of propagation of velocity disturbances, first investigated by Eckelmann [21]. These experimental results have been confirmed firstly by Kim and Hussain [22] in DNS simulation of a flat-plate turbulent boundary layer. They calculated the celerity of propagation of velocity disturbances near a wall from the time lag of the correlation peak between time histories of streamwise aligned pairs of points separated by a known distance. Del Alamo and Jimenez [23] and Geng et al. [24] also confirmed these findings by looking for the celerity that minimizes the discrepancy between their velocity data and what is supposed by the Taylor hypothesis. The average convection velocity of velocity events is determined from the local time and space derivatives of the velocity field components according to the Taylor hypothesis, and it is found to be proportional to the friction velocity [25-28]. The relationship between the celerity of displacement of temperature disturbances and the friction velocity was investigated in [28]. Based on these observations, Miozzi et al. [17-20] inferred the friction velocity and the friction coefficient on the basis of the celerity of propagation of temperature disturbances.

In this paper, we discuss the relationship between skin friction and the surface optical flow (SOF) of the surface scalars (defined as an equivalent or modeled convection velocity) based on the evolution equations of the surface scalars themselves. The evolution equations of the surface temperature and passive scalar were obtained by Liu et al. [15, 29, 30] and Chen et al. [14]. Recently, Chen et al. [31] obtained the evolution equation of the surface enstrophy in wall-bounded flows. These evolution equations can be written in a generic form where the SOF of a scalar quantity (surface temperature, relative concentration or enstrophy) is related to skin friction and other relevant parameters. When the effects of other parameters (such as surface curvature and third-order wall-normal derivatives) are small, the celerity of the scalar quantity is approximately proportional to skin friction. Since the evolution equations can be re-cast to the optical flow equation, the SOF can be determined using a variational method as an optical flow problem. As an example, a dataset of direct numerical simulation (DNS) of a turbulent channel flow is used to evaluate the correlation between the SOF of the enstrophy and skin friction. Further, the fields of the SOF are calculated from temperature sensitive paint (TSP) data of a National Advisory Committee for Aeronautics (NACA) 0015 airfoil model obtained in wind tunnel testing, and compared with the skin friction data obtained in global luminescent oil-film (GLOF) skin friction measurements. The developed method is further evaluated in TSP measurements in an impinging jet.

2. Evolution equations of surface scalar quantities

2.1. Temperature

The relation between the skin friction vector $\boldsymbol{\tau}$ and the surface temperature T_w was derived from the energy equation by Liu et al. [15] and Chen et al. [14]. This relation is written as

$$\boldsymbol{\tau}\cdot\nabla T_w = \frac{\mu}{k}\left(\frac{\partial}{\partial t} - a\nabla^2\right)q_w + \varepsilon_T, \tag{1}$$

where the virtual source term is given by

$$\begin{aligned}\varepsilon_T = {} & \frac{\mu^2}{\rho c}\left[\frac{\partial \Phi}{\partial x_3}\right]_w - a\mu Tr(\boldsymbol{K})\left[\frac{\partial^2 T}{\partial x_3^2}\right]_w + a\mu\left[\frac{\partial^3 T}{\partial x_3^2}\right]_w \\ & + a\mu\left[\boldsymbol{K}:\boldsymbol{K}q_w/k + 2Tr\left(\nabla\nabla T_w\cdot\boldsymbol{K}\right) + \left(\nabla\cdot\boldsymbol{K}\right)\cdot\left(\nabla T_w\right)\right]\end{aligned}, \tag{2}$$

In Eqs. (1)-(2), the subscript w denotes physical properties at a surface (wall), $\nabla = \partial/\partial x_i$ ($i = 1,2$) is a gradient operator on a surface, x_3 is the wall-normal coordinate, ρ is the density of the fluid, c is the specific heat at constant volume, T is the temperature, μ is the dynamic viscosity, Φ is the dissipation function, $a = k/\rho c$ is the thermal diffusivity, $\boldsymbol{K}$ is the surface curvature tensor, Tr denotes the trace of a second-order tensor, and $q_w = -k\left[\partial T/\partial x_3\right]_w$ is the heat flux on the surface which is positive when the heat enters into fluid from the surface. In Eq. (2), the first term in the RHS represents the wall-normal diffusion of the viscous dissipation function Φ, and the second and fourth terms represent the effect of the curvature on the heat flux and surface temperature gradient. The third term represents the effect of the third-order wall-normal derivative of temperature at a wall.

We consider a temperature sensitive paint (TSP) layer on a heated base (model). The

heat flux q_w is modeled by $q_w = h_T\left(T_0 - T_w\right)$, where h_T is a convection heat transfer coefficient that is position-dependent but time-independent and T_0 is the surface temperature without flow. Therefore, Eq. (1) is written as

$$\partial T_w / \partial t + \left(k / \mu h_T\right)\left(\boldsymbol{\tau} \cdot \nabla T_w - \varepsilon_T\right) = a\nabla^2 T_w . \tag{3}$$

The second term in the left-hand-side (LHS) of Eq. (3) is dominated by the gradient term $\boldsymbol{\tau} \cdot \nabla T_w$, while ε_T is a relatively smaller but complex term in most cases. To simplify Eq. (3) formally, a transport model for ε_T is proposed, i.e., $\varepsilon_T \equiv \gamma_T \boldsymbol{\tau} \cdot \nabla T_w$, where γ_T is an non-dimensional effective thermal diffusivity along a skin friction line. Thus, a transport model for the second term in the LHS of Eq. (3) is

$$\left(k / \mu h_T\right)\left(\boldsymbol{\tau} \cdot \nabla T_w - \varepsilon_T\right) \equiv \boldsymbol{u}_T \cdot \nabla T_w , \tag{4}$$

where $\boldsymbol{u}_T$ is the surface optical flow (SOF), defined as an equivalent or modeled convection velocity of a surface temperature event, i.e.,

$$\boldsymbol{u}_T = \left(k / \mu h_T\right)\left(1 - \gamma_T\right)\boldsymbol{\tau} . \tag{5}$$

The unit of $\boldsymbol{u}_T$ is ms^{-1}. Therefore, Eq. (3) is written as an evolution equation

$$\partial T_w / \partial t + \boldsymbol{u}_T \cdot \nabla T_w = a\nabla^2 T_w . \tag{6}$$

For a low-speed flow over a surface with a small curvature, the term ε_T can be neglected and thus the SOF is $\boldsymbol{u}_T = \left(k / \mu h_T\right)\boldsymbol{\tau}$. In the above derivations, the first assumption is $q_w = h_T\left(T_0 - T_w\right)$ that is traditionally used in heat transfer studies, where the convection heat transfer coefficient h_T is introduced. The second assumption is $\varepsilon_T \equiv \gamma_T \boldsymbol{\tau} \cdot \nabla T_w$, where the non-dimensional effective thermal diffusivity γ_T is introduced to describe ε_T as a gradient diffusion of ∇T_w along a skin friction line. There assumptions are reasonable since the

diffusion is a main process on the surface. When the holistic parameters h_T and γ_T are not constant, the proportional relation between $\boldsymbol{u}_T$ and $\boldsymbol{\tau}$ could be position-dependent.

The surface temperature and SOF are decomposed into the mean term and fluctuation, i.e., $T_w = \langle T_w \rangle + T_w'$ and $\boldsymbol{u}_T = \langle \boldsymbol{u}_T \rangle + \boldsymbol{u}_T'$, where $\langle\ \rangle$ is an ensemble averaging or time averaging operator and the prime denotes fluctuation. In the statistically stationary state, the mean equation is

$$\langle \boldsymbol{u}_T \rangle \cdot \nabla \langle T_w \rangle = a \nabla^2 \langle T_w \rangle - \langle \boldsymbol{u}_T' \cdot \nabla T_w' \rangle, \tag{7}$$

where the correlation term $-\langle \boldsymbol{u}_T' \cdot \nabla T_w' \rangle$ represents the transport of the surface temperature fluctuation by the SOF fluctuation. The equation for the surface temperature fluctuation energy $e_T = T_w'^2 / 2$ is

$$\frac{\partial e_T}{\partial t} + \boldsymbol{u}_T \cdot \nabla e_T = a T_w' \nabla^2 T_w' + T_w' \langle \boldsymbol{u}_T' \cdot \nabla T_w' \rangle - T_w' \boldsymbol{u}_T' \cdot \nabla \langle T_w \rangle, \tag{8}$$

where the fluctuating terms in Eq. (8) act as a source term. Theoretically, the effect of the source term could be considered by the iteration procedure of the optical flow method.

2.2. Scalar

We consider the binary mass diffusion equation with a source term, *i.e.*, [29, 30]

$$\partial \phi / \partial t + \boldsymbol{u} \cdot \nabla \phi = D_{12} \nabla^2 \phi + Q_s, \tag{9}$$

where $\phi = \rho_1 / \rho$ is the relative concentration (density) of the species 1, $\rho = \rho_1 + \rho_2$ is the total density of the binary gas, D_{12} is the diffusivity of a binary system, Q_s is the source term, and $\boldsymbol{u}$ is the fluid velocity. According to Liu et al. [29, 30] and Chen et al. [14], the

relation between the skin friction vector $\boldsymbol{\tau}$ and the surface temperature ϕ_w is given by

$$\boldsymbol{\tau}\cdot\nabla\phi_w = \frac{\mu}{D_{12}\rho_w}\left(\frac{\partial}{\partial t} - D_{12}\nabla^2\right)\dot{m}_{1w} + \varepsilon_\phi\,, \tag{10}$$

where the virtual source term is written as

$$\begin{aligned}\varepsilon_\phi = {} & \mu\left[\frac{\partial Q_s}{\partial x_3}\right]_w - \mu D_{12}Tr\left(\boldsymbol{K}\right)\left[\frac{\partial^2\phi}{\partial x_3^2}\right]_w + \mu D_{12}\left[\frac{\partial^3\phi}{\partial x_3^2}\right]_w \\ & +\mu\left[\boldsymbol{K}:\boldsymbol{K}\dot{m}_{1w}/\rho_w + 2D_{12}Tr\left(\nabla\nabla\phi_w\cdot\boldsymbol{K}\right) + D_{12}\left(\nabla\cdot\boldsymbol{K}\right)\cdot\left(\nabla\phi_w\right)\right]\end{aligned}\,. \tag{11}$$

In Eqs. (10)-(11), $\dot{m}_{1w} = -D_{12}\rho_w\left[\partial\phi/\partial x_3\right]_{\partial w}$ is the diffusive flux of species 1 on the surface, which is positive when the scalar diffuses into fluid. The physical meanings of the terms in Eq. (11) correspond to those in Eq. (2).

We consider two methods for mass transfer visualizations: PSP and sublimation coating. Pressure sensitive paint (PSP) is used as an oxygen sensor for surface mass-transfer visualizations in low-speed flows [29]. If nitrogen is added in flow as the species 1 that diffuses into a PSP polymer layer to purge the oxygen (the species 2) in the layer, PSP will emit the stronger luminescence due to the reduced oxygen quenching. In the other case where oxygen is injected to flow, the luminescent emission from PSP will be quenched. At the interface between the gas flow and PSP, the mass transfer flux is modeled by $\dot{m}_{1w} = h_M\,\rho_w(\phi_0 - \phi_w)$, where ϕ_w and ϕ_0 are the values of ϕ at the gas-PSP interface with and without flow, respectively, and h_M is a mass transfer coefficient that is position-dependent but time-independent. This model is also applicable to sublimation coating. Therefore, Eq. (10) is written as an evolution equation

$$\partial\phi_w/\partial t + \left(D_{12}/\mu h_M\right)\left(\boldsymbol{\tau}\cdot\nabla\phi_w - \varepsilon_\phi\right) = D_{12}\nabla^2\phi_w\,. \tag{12}$$

Similar to the heat transfer problem, a transport model is

$$\left(D_{12}/\mu h_M\right)\left(\boldsymbol{\tau}\cdot\nabla\phi_w-\varepsilon_\phi\right)\equiv\boldsymbol{u}_\phi\cdot\nabla\phi_w\,, \tag{13}$$

Therefore, Eq. (12) is written as an evolution equation

$$\partial\phi_w/\partial t+\boldsymbol{u}_\phi\cdot\nabla\phi_w=D_{12}\nabla^2\phi_w\,, \tag{14}$$

where $\boldsymbol{u}_\phi$ is the SOF of a surface scalar structure. Further, when a mass diffusion model $\varepsilon_\phi\equiv\gamma_M\boldsymbol{\tau}\cdot\nabla\phi_w$ along a skin friction is used, the SOF is

$$\boldsymbol{u}_\phi=\left(D_{12}/\mu h_M\right)\left(1-\gamma_M\right)\boldsymbol{\tau}\,, \tag{15}$$

where γ_M is the non-dimensional effective mass diffusivity. The unit of $\boldsymbol{u}_\phi$ is ms^{-1}.

The relative surface scalar concentration and SOF are decomposed into the mean term and fluctuation, i.e., $\phi_w=\langle\phi_w\rangle+\phi'_w$ and $\boldsymbol{u}_\phi=\langle\boldsymbol{u}_\phi\rangle+\boldsymbol{u}'_\phi$. In the statistically stationary state, the mean equation is

$$\langle\boldsymbol{u}_\phi\rangle\cdot\nabla\langle\phi_w\rangle=D_{12}\nabla^2\langle\phi_w\rangle-\langle\boldsymbol{u}'_\phi\cdot\nabla\phi'_w\rangle\,, \tag{16}$$

where the correlation term $-\langle\boldsymbol{u}'_\phi\cdot\nabla\phi'_w\rangle$ represents the transport of the surface scalar fluctuation by the SOF fluctuation. The equation for the surface scalar fluctuation energy $e_\phi=\phi'^2_w/2$ is

$$\frac{\partial e_\phi}{\partial t}+\boldsymbol{u}_\phi\cdot\nabla e_t=D_{12}\phi'_w\nabla^2\phi'_w+\phi'_w\langle\boldsymbol{u}'_\phi\cdot\nabla\phi'_w\rangle-\phi'_w\boldsymbol{u}'_\phi\cdot\nabla\langle\phi_w\rangle\,, \tag{17}$$

where the fluctuating terms in Eq. (17) act as a source term.

2.3. Enstrophy

According to Chen et al. [31], the relation between the skin friction vector $\boldsymbol{\tau}$ and the surface enstrophy Ω_w is given by

$$2\boldsymbol{\tau}\cdot\nabla\Omega_w=-\left(\frac{\partial}{\partial t}-\nu\nabla^2\right)f_\Omega+\varepsilon_\Omega\,, \tag{18}$$

where the virtual source term is written as

$$\varepsilon_\Omega = \nu\left[\frac{\partial^2 F_\Omega}{\partial x_3^2}\right]_w + 2(\nabla\cdot\boldsymbol{\tau})\Omega_w - \frac{2}{\rho}(\nabla\boldsymbol{\tau}):(\nabla\nabla p_w) - \frac{2}{\mu}\left[\left(\frac{\partial}{\partial t} - \nu\nabla^2\right)\boldsymbol{\tau}\right]\cdot(\nabla p_w) \quad (19)$$

In Eqs. (18)-(19), $\Omega = |\boldsymbol{\omega}|^2/2$ is the enstrophy, $F_\Omega = \mu\partial\Omega/\partial x_3$ is the wall-normal enstrophy flux, $f_\Omega = \mu[\partial\Omega/\partial x_3]_w$ is the boundary enstrophy flux (BEF) that is negative when Ω diffuses into fluid, and the subscript *w* denotes the quantity at a wall. In an attached flow region, f_Ω is usually negative, but it could be positive in some limited regions near separation lines and critical points. In Eq. (19), the first term represents the effect of the second derivative of the enstrophy flux in the wall-normal direction, the second term represents the effect of the skin friction divergence, the third term represents the interaction between the skin friction gradient and the surface pressure Hessian, and the fourth term represents the interaction of the skin friction source term and surface pressure gradient. Chen et al. [11] found that $2\boldsymbol{\tau}\cdot\nabla\Omega_w$ was a major term in 3D viscous flows particularly near separation and attachment lines although these terms in ε_Ω had some effects. It is noted that the surface enstrophy Ω_w is proportional to the dissipation rate at a wall [11].

Based on an analogy to a typical diffusion process of a scalar (temperature or concentration), a diffusion model for the enstrophy is proposed, i.e., $f_\Omega = h_\Omega(\Omega_0 - \Omega_w)$, where h_Ω is an enstrophy transfer coefficient that is position-dependent but time-independent and Ω_0 is the enstrophy without flow (zero). Therefore, Eq. (18) is written as an evolution equation

$$\partial\Omega_w / \partial t + \left(1/h_\Omega\right)\left(\varepsilon_\Omega - 2\boldsymbol{\tau}\cdot\nabla\Omega_w\right) = \nu\nabla^2\Omega_w . \tag{20}$$

A transport model is given by

$$\left(1/h_\Omega\right)\left(\varepsilon_\Omega - 2\boldsymbol{\tau}\cdot\nabla\Omega_w\right) \equiv \boldsymbol{u}_\Omega\cdot\nabla\Omega_w . \tag{21}$$

Therefore, an evolution equation is

$$\partial\Omega_w / \partial t + \boldsymbol{u}_\Omega\cdot\nabla\Omega_w = \nu\nabla^2\Omega_w , \tag{22}$$

where $\boldsymbol{u}_\Omega$ is the SOF of a surface enstrophy structure. In particular, when a diffusion model $\varepsilon_\Omega \equiv \gamma_\Omega\boldsymbol{\tau}\cdot\nabla\Omega_w$ is used where γ_Ω is the non-dimensional effective diffusion coefficient, the SOF is

$$\boldsymbol{u}_\Omega = \left(1/h_\Omega\right)\left(\gamma_\Omega - 2\right)\boldsymbol{\tau} . \tag{23}$$

Since ε_Ω and $\boldsymbol{\tau}\cdot\nabla\Omega_w$ are in the same order, the SOF $\boldsymbol{u}_\Omega$ depends on not only skin friction but also the effects of the terms in Eq. (19). The unit of $\boldsymbol{u}_\Omega$ is ms^{-1}.

The surface enstrophy and SOF are decomposed into the mean term and fluctuation, i.e., $\Omega_w = \left\langle\Omega_w\right\rangle + \Omega_w'$ and $\boldsymbol{u}_\Omega = \left\langle\boldsymbol{u}_\Omega\right\rangle + \boldsymbol{u}_\Omega'$. The mean equation is

$$\left\langle\boldsymbol{u}_\Omega\right\rangle\cdot\nabla\left\langle\Omega_w\right\rangle = \nu\nabla^2\left\langle\Omega_w\right\rangle - \left\langle\boldsymbol{u}_\Omega'\cdot\nabla\Omega_w'\right\rangle . \tag{24}$$

The equation for the surface enstrophy fluctuation energy $e_\Omega = \Omega_w'^2/2$ is

$$\frac{\partial e_\Omega}{\partial t} + \boldsymbol{u}_\Omega\cdot\nabla e_\Omega = \nu\,\Omega_w'\nabla^2\Omega_w' + \Omega_w'\left\langle\boldsymbol{u}_\Omega'\cdot\nabla\Omega_w'\right\rangle - \Omega_w'\boldsymbol{u}_\Omega'\cdot\nabla\left\langle\Omega_w\right\rangle . \tag{25}$$

where the fluctuating terms in Eq. (22) act as a source term.

The SOF of the surface enstrophy can also be derived by applying the enstrophy equation to the wall (see Appendix), namely,

$$\boldsymbol{u}_\Omega\cdot\nabla\Omega_w = S_\Omega , \tag{26}$$

where the source term is

$$S_\Omega = \nu \nabla \boldsymbol{\omega}_w : \nabla \boldsymbol{\omega}_w + \frac{1}{\rho^2 \nu} |\nabla p_w|^2 + \nu |\nabla \cdot \boldsymbol{\omega}_w|^2 - \nu \left[\frac{\partial^2 \Omega}{\partial x_3^2} \right]_w . \tag{27}$$

The first, second and third terms in Eq. (27) represent the contributions of the surface dissipation rate at a wall, surface pressure gradient magnitude and surface vorticity divergence, respectively. Eq. (26) indicates that the SOF $\boldsymbol{u}_\Omega$ depends on these terms. In this sense, $\boldsymbol{u}_\Omega$ represents the several physical mechanisms on a wall in a viscous flow.

2.4. Relations between the SOFs of different quantities

In this paper, the SOF $\boldsymbol{u}_T$, $\boldsymbol{u}_\phi$ or $\boldsymbol{u}_\Omega$ is defined as the convection velocity of the surface temperature, scalar or enstrophy in the corresponding evolution equation. According to Eqs. (5) and (15), a relation between the SOFs of temperature and scalar is

$$\boldsymbol{u}_T = \left(\frac{Sh}{Nu} \right) \left(\frac{1-\gamma_T}{1-\gamma_M} \right) \boldsymbol{u}_\phi , \tag{28}$$

where $Sh = h_M L / D_{12}$ is the Sherwood number, $Nu = h_T L / k$ is the Nusselt number, and L is a characteristic length. The heat transfer coefficient h_T and mass transfer coefficient h_M are empirical coefficients depending on flow conditions. The thermal and mass transfer diffusivies γ_T and γ_M are also empirical coefficients in the diffusion models $\varepsilon_T \equiv \gamma_T \boldsymbol{\tau} \cdot \nabla T_w$ and $\varepsilon_\phi \equiv \gamma_M \boldsymbol{\tau} \cdot \nabla \phi_w$ along a skin friction line, respectively. Therefore, γ_T and γ_M are the holistic parameters describing the effects of ε_T and ε_ϕ collectively. According to Eqs. (5) and (23), a relation between the SOFs of temperature and enstrophy is

$$\boldsymbol{u}_T = \left(\frac{En}{Nu} \right) \left(\frac{1-\gamma_T}{\gamma_\Omega - 2} \right) \boldsymbol{u}_\Omega , \tag{29}$$

where $En = h_\Omega L / \mu$ is a non-dimensional number describing the ratio of the enstrophy diffusion coefficient to the fluid viscosity at a surface, and γ_Ω is a diffusion coefficient to describe the effects of ε_Ω.

3. Determining SOF

The evolution equations, Eqs. (6), (8), (14), (17), (22) and (25), enjoy the same mathematical form. The gradient operator and Laplace operator in these equations can be transformed and expressed in the image coordinates by using the orthographical projection transformation. Theses equations can be written as a generic form of the optical flow equation, i.e.,

$$\partial g / \partial t + \boldsymbol{u} \cdot \nabla g = f , \tag{30}$$

where g is a generic measured quantity (temperature, scalar or enstrophy), $\boldsymbol{u}$ is the surface optical flow (SOF), f is the right-hand-side term (the source term) and $\nabla = \partial / \partial x_i$ $(i = 1,2)$ is the gradient operator in the image plane.

In principle, when g and f are known from measurements, Eq. (30) can be solved as an inverse problem for the optical flow $\boldsymbol{u}$ [32, 33]. To solve Eq. (30), the variational method is applied by minimizing the residue functional

$$J(\boldsymbol{u}) = \| \partial g / \partial t + \boldsymbol{u} \cdot \nabla g - f \|_2 + \alpha \left\| |\nabla u_1|^2 + |\nabla u_2|^2 \right\|_2 , \tag{31}$$

where $\| \|_2$ denotes the L2 norm on a domain D and α is a Lagrange multiplier (a regularization parameter). The first term in $J(\boldsymbol{u})$ is the equation term, and the second term is a regularization functional as a smoothness constraint assuming that a skin friction field is

sufficiently continuous and smooth. Therefore, the Euler-Lagrange equation is obtained, i.e.,

$$[\,\partial g/\partial t+\boldsymbol{u}\cdot\nabla g-f\,]\nabla g-\alpha\nabla^2\boldsymbol{u}=0\,, \tag{32}$$

where $\nabla=\partial/\partial x_i$, $\nabla^2=\partial^2/\partial x_i\partial x_i$ $(i=1,2)$, and α is a Lagrange multiplier. Eq. (32) can be solved numerically with the Neumann condition $\partial\boldsymbol{u}/\partial n=0$ imposed on the domain boundary [32, 33]. The mathematical analysis on the uniqueness and convergence of the solution of Eq. (32) is given by Aubert et al. [34, 35] and Wang et al. [36].

In an error analysis, the decompositions $g=g_0+\delta g$, $g_t=\partial g/\partial t=g_{t0}+\delta g_t$, $f=f_0+\delta f$, and $\boldsymbol{u}=\boldsymbol{u}_0+\delta\boldsymbol{u}$ are introduced, where δg, δg_t, δf and $\delta\boldsymbol{u}$ are errors, and g_0, g_{t0}, f_0 and $\boldsymbol{u}_0$ are the non-perturbed fields that exactly satisfy Eq. (30). Substituting the above decompositions into Eq. (32) and neglecting the higher-order small terms, we have an error propagation equation

$$(\delta\boldsymbol{u}\cdot\nabla g_0)\nabla g_0-\alpha\nabla^2\delta\boldsymbol{u}=-(\delta g-\delta f+\boldsymbol{u}_0\cdot\nabla\delta g)\nabla g_0\,, \tag{33}$$

where δg and δf directly contribute to the error $\delta\boldsymbol{u}$.

In a local linear approximation, we consider a local region where ∇g_0 is a constant vector with the magnitude $\|\nabla g_0\|$, and introduce the unit normal vector to an iso-value line $g_0=const.$ i.e., $\boldsymbol{N}_T=\nabla g_0/\|\nabla g_0\|$. The skin friction error projected on $\boldsymbol{N}_T$ is defined as $(\delta\boldsymbol{u})_N=\delta\boldsymbol{u}\cdot\boldsymbol{N}_T$. From Eq. (33), a formal estimate of the relative error is obtained, i.e.,

$$\frac{(\delta\boldsymbol{u})_N}{\|\boldsymbol{u}_0\|}=-\frac{\delta g-\delta f}{\|\nabla g_0\|\|\boldsymbol{u}_0\|}-\left(\frac{\boldsymbol{u}_0}{\|\boldsymbol{u}_0\|}\right)\cdot\delta\boldsymbol{N}_T+\frac{\alpha}{\|\nabla g_0\|^2}\nabla^2\left[\frac{(\delta\boldsymbol{u})_N}{\|\boldsymbol{u}_0\|}\right], \tag{34}$$

where $\|\boldsymbol{u}_0\|$ is a characteristic value of the optical flow (e.g. the mean value). The first term in the RHS of Eq. (34) is the contribution from δg and δf, and the second term is the contribution from the elemental error in measurement of the surface gradient of the intensity

g. The third term represents the artificial diffusion of the error $(\delta \boldsymbol{u})_N$ associated with the Lagrange multiplier.

Since the first and third terms in the RHS of Eq. (34) is proportional to $\|\nabla g_0\|^{-1}$ and $\|\nabla g_0\|^{-2}$, respectively, the relative error $(\delta \boldsymbol{u})_N / \|\boldsymbol{u}_0\|$ increases as $\|\nabla g_0\|$ decreases. The proportional factor $\alpha \|\nabla g_0\|^{-2}$ in the third term is interesting. It is indicated that when $\|\nabla g_0\|$ is small the Lagrange multiplier α should be sufficiently small to reduce the error. On the other hand, for an ill-posed problem, the variational solution with the Lagrange multiplier α is affected by the data error bounded by a positive number δ. The selected value of α depends on δ, i.e., $\alpha = \alpha(\delta)$. The error of the solution is proportional to $\delta / \sqrt{\alpha}$ as $\delta \to 0$ [37, 38]. The condition for the solution convergence is $\delta^2 / \alpha(\delta) \to 0$, indicating that the data error must be reduced when α is small. Therefore, two conflicting requirements exit in the case. In the regions where $\|\nabla g_0\|$ is small, α should be small based on Eq. (34), and accordingly the data error bound δ must be tightly controlled to insure the accuracy of the solution. From this perspective, there may be the optimum value of the Lagrange multiplier. No rigorous theory is available to determine a priori the optimum value of the Lagrange multiplier. The selection of the Lagrange multiplier is a trial-and-error procedure based on simulations for a specific application.

4. SOF of enstrophy in turbulent channel flow

To examine the relationship between skin friction and the SOF of enstrophy, the dataset of direct numerical simulation (DNS) of a turbulent channel flow is used. This is a

challenging case for the optical flow method to apply to a pseudo-random near-wall flow where coherent structures and small-scale random structures are mixed. DNS of a turbulent channel flow at the frictional Reynolds number 180 was performed using a multi-relaxation-time lattice Boltzmann method (MRT-LBM), which can be viewed as a weakly compressible NS solver in the continuum limit [11]. A single-phase turbulent channel flow was considered with x, y, and z representing streamwise, wall-normal, and spanwise directions, respectively. The domain size is L_x in the streamwise direction and L_z in the spanwise direction. The half channel width is H ($L_y = 2H$). In lattice units, $L_x = 1800$, $L_z = 600$, and $L_y = 299$. Three hundred lattice points were used in the wall-normal direction with the first and the last points located at the bottom and top stationary walls, respectively. The near-wall flow structures in this turbulent channel flow were discussed by Chen et al. [11]

Figure 1 shows a typical pair of instantaneous surface enstrophy fields (Ω_w) normalized by its maximum value with a time interval of 100 time steps in lattice units between them, where one pixel corresponds to 1.204 viscous wall length unit. Figure 2 shows the corresponding skin friction lines and skin friction magnitude field. Skin friction was directly computed by MRT-LBM without using the standard numerical differentiation at a wall [11]. These results reveal the physical features of complex near-wall flow structures, in particular the streaky features associated with quasi-streamwise vortices above the viscous sublayer [11]. A typical strong wall-normal velocity event (SWNVE) is identified, which is enclosed in the region of interest marked in Fig. 1. The concentrated enstrophy and dissipation are associated with the SWNVE and high skin friction magnitude. It is found that the SWNVE is

dynamically important in generating the boundary enstrophy flux, greatly enhancing the intermittency of turbulence inside the viscous sublayer.

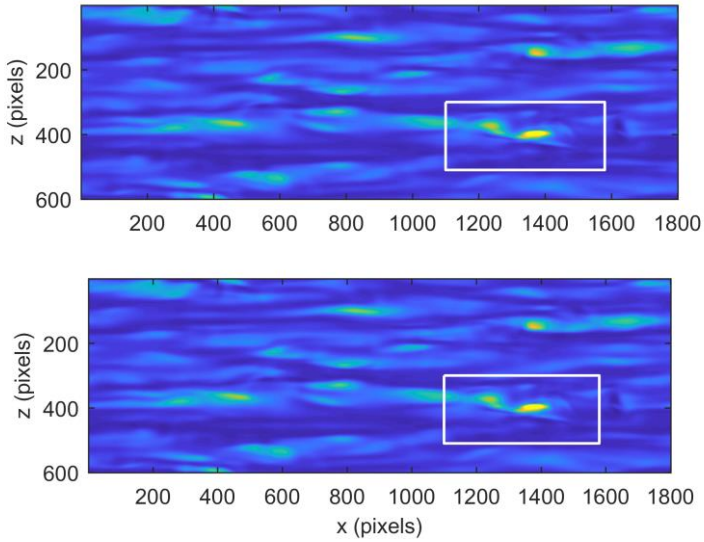

Figure 1. A pair of surface enstrophy fields normalized by its maximum value at $t = 0$ (above) and $t = 100$ time steps in lattice units (below).

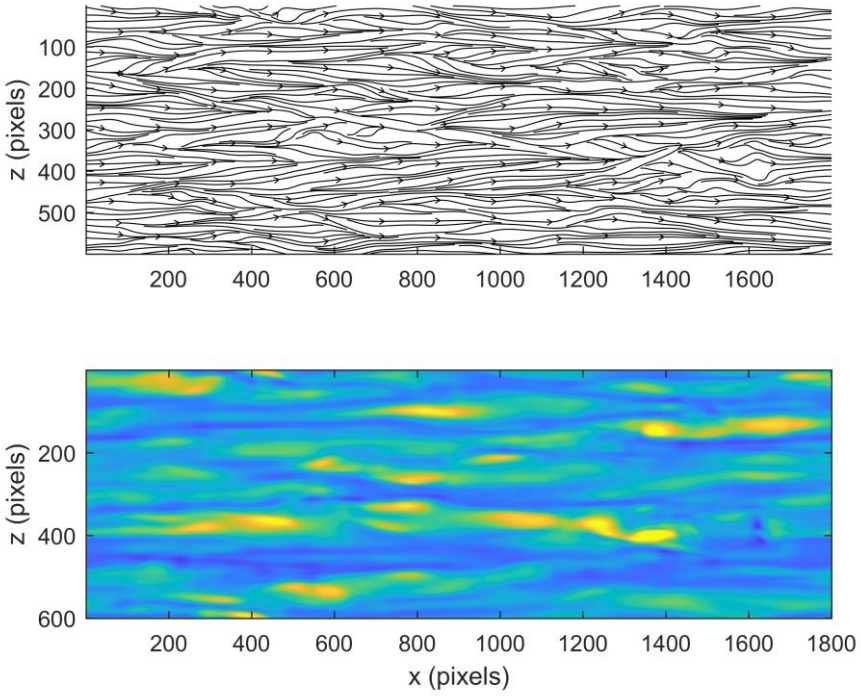

Figure 2. Skin friction lines (above) and skin friction magnitude field normalized by its maximum value (below).

From sequential surface enstrophy fields, the SOF of enstrophy $\boldsymbol{u}_\Omega$ is calculated by solving Eq. (32) where the Lagrange multiplier is $\alpha = 1$ and the source term is $f = 0$. Simulations indicate that the extracted results are not sensitive to the selection of the Lagrange multiplier in a range of $\alpha = 0.1 - 500$. Figure 3 shows streamlines lines of the SOF of enstrophy and its magnitude field normalized by its maximum value, which are extracted from the images in Fig. 1. The correlation coefficient between the magnitudes $|\boldsymbol{u}_\Omega|$ and $|\boldsymbol{\tau}|$ in the whole domain is calculated, which is shown in Fig. 4(a) as a function of the maximum displacement between two consecutive surface enstrophy images, where $|\boldsymbol{\tau}|$ was directly computed by MRT-LBM [11]. When the maximum displacement is larger than 3 pixels, the correlation coefficient is about 0.48. The angular cosine $\cos(\theta) = \boldsymbol{u}_\Omega \cdot \boldsymbol{\tau} / |\boldsymbol{u}_\Omega||\boldsymbol{\tau}|$ is calculated to estimate the angular difference θ between $\boldsymbol{u}_\Omega$ and $\boldsymbol{\tau}$. The standard deviation (std) of $\cos(\theta)$ is shown in Fig. 4(b) as a function of the maximum displacement. Since the mean of $\cos(\theta)$ is one, the relative error of $\cos(\theta)$ is about 23% when the maximum displacement is large. Figures 5(a) and 5(b) show the probability density functions (PDFs) of skin friction given by DNS and the SOF extracted in the measurement domain. The PDFs of the *x*-components (the streamwise components) of skin friction and the SOF exhibit the non-symmetrical distribution with the positive skewness (skewed toward the right side). The PDF of the *x*-component of the SOF has a larger tail compared to that of skin friction given by DNS. For reference, the PDF of skin friction obtained from hot-film measurements in a flat-plate turbulent boundary layer at the Reynolds number of 2,900 based on the momentum thickness is also plotted in Fig. 5(a) [26]. The PDF calculated from a time series of hot-film

data at a fixed location is consistent with those calculated from the domain. Figure 5(b) shows the near-symmetrical PDFs of the *y*-components of skin friction and the SOF. The PDF of the *y*-component of the SOF with the kurtosis of 3.92 is close to a Gaussian distribution. In contrast, the DNS data shows a more spiky distribution with the kurtosis of 7.41.

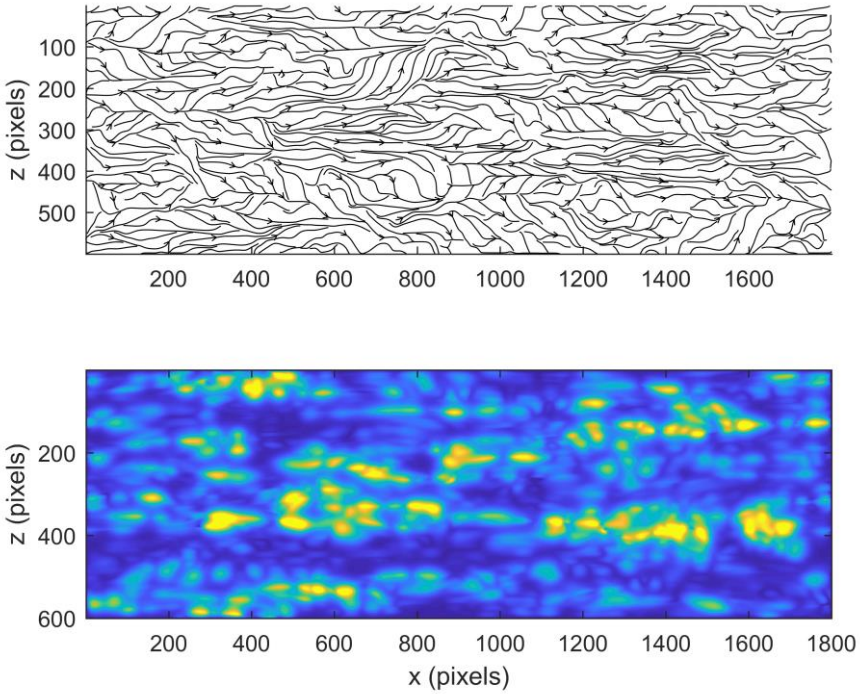

Figure 3. Streamlines lines of the SOF of enstrophy (above) and its magnitude field normalized by its maximum value (below), which are extracted from the images in Fig. 1.

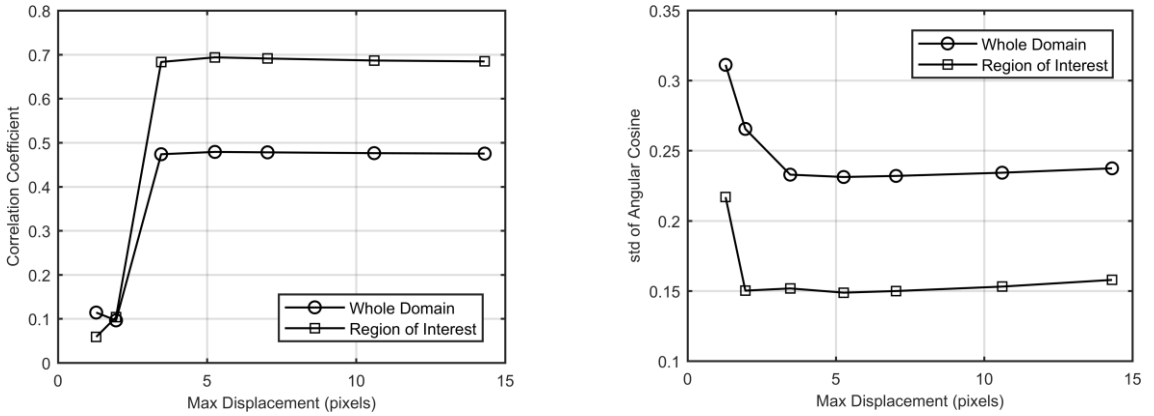

(a) (b)

Figure 4. (a) The correlation coefficient between the magnitudes $|\boldsymbol{u}_\Omega|$ and $|\boldsymbol{\tau}|$ and (b) the std of the angular cosine as a function of the maximum displacement between two consecutive surface enstrophy images for the Lagrange multiplier of 2.

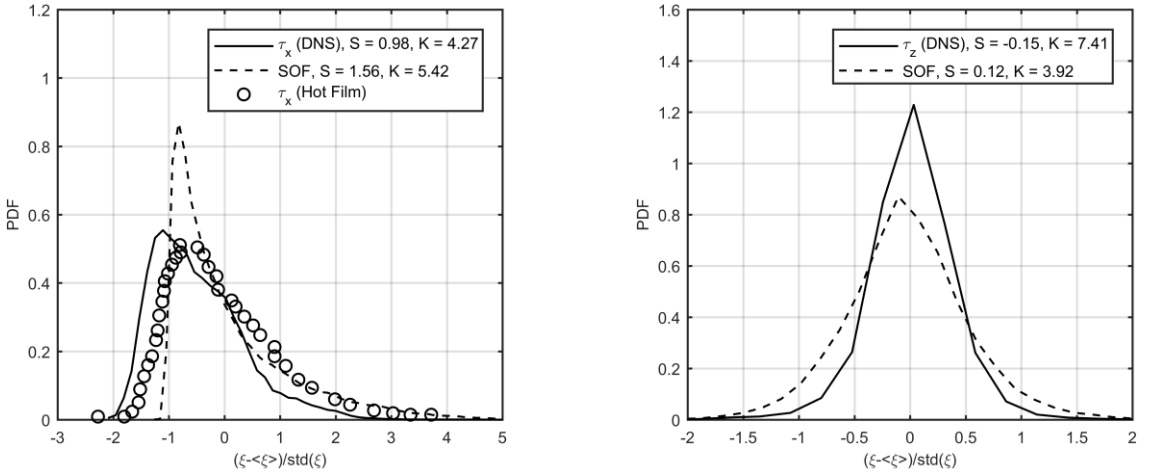

(a) (b)

Figure 5. Probability density functions (PDFs) of skin friction and the SOF: (a) *x*-components of skin friction and the SOF, and (b) *z*-components of skin friction and the SOF, where the hot-film skin friction data are extracted from Reference 26. S and K denote the skewness and kurtosis, respectively.

Further, a typical SWNVE in the region of interest (ROI) in Fig. 1 is examined closely. Figures 6 and 7 show the results of the skin friction vector $\boldsymbol{\tau}$ and the SOF of enstropy $\boldsymbol{u}_\Omega$ in the ROI. The correlation coefficient between the magnitudes $|\boldsymbol{u}_\Omega|$ and $|\boldsymbol{\tau}|$ in the region of interest is about 0.69 when the maximum displacement is larger than 3 pixels. Although the structure of $\boldsymbol{u}_\Omega$ exhibits a pattern similar to the structure of $\boldsymbol{\tau}$, there is a significant amount of dissimilarity between $\boldsymbol{u}_\Omega$ and $\boldsymbol{\tau}$. This dissimilarity is due to the fact that $\boldsymbol{u}_\Omega$ depends on not only $\boldsymbol{\tau}$, but also the effects of the surface dissipation rate, surface pressure gradient magnitude and surface vorticity divergence (see Section 2.3 and Appendix). Secondly, this dissimilarity is caused by the error in optical flow computation in the region where the image intensity gradient magnitude $\|\nabla g_0\|$ is small. In a region where $\|\nabla g_0\|$ is large (such as the ROI in Fig. 1), the structure of $\boldsymbol{u}_\Omega$ is more similar to that of $\boldsymbol{\tau}$. Figure 8(a) shows the correlation coefficient between the magnitudes $|\boldsymbol{u}_\Omega|$ and $|\boldsymbol{\tau}|$ in the ROI as a function of the Lagrange multiplier for the maximum displacement of 7 pixels between two consecutive surface enstrophy images. The correlation coefficient increases gradually with the Lagrange multiplier until reaching a relatively stable value. The std of $\cos(\theta)$ in the ROI is shown in Fig. 8(b) as a function of the Lagrange multiplier. The relative error of $\cos(\theta)$ increases to about 22% from7% with the Lagrange multiplier.

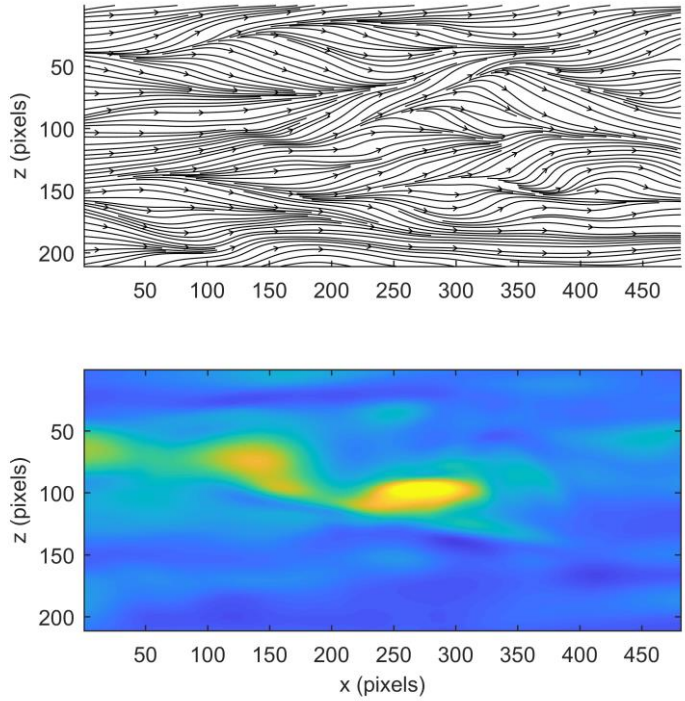

Figure 6. Skin friction lines (above) and skin friction magnitude field normalized by its maximum value (below) in the region of interest.

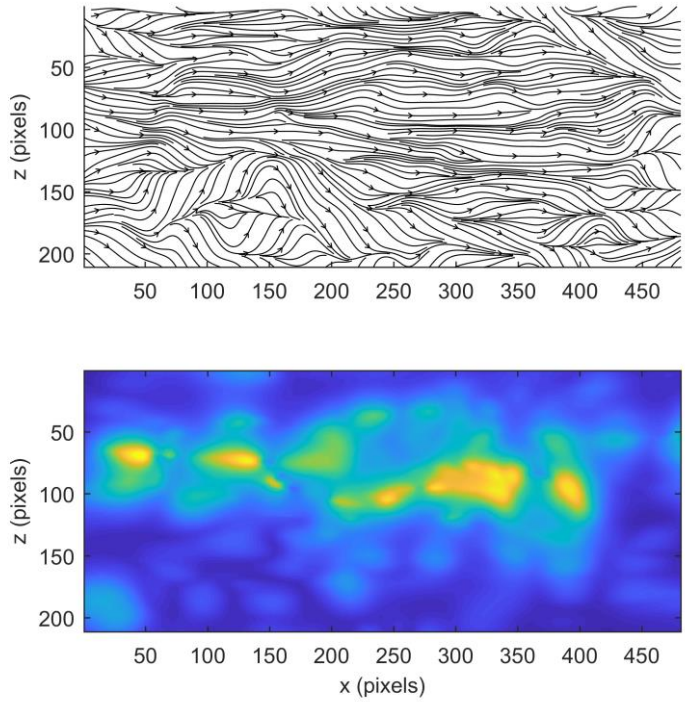

Figure 7. Streamlines lines of the SOF of enstrophy (above) and magnitude field normalized by its maximum value (below) in the region of interest.

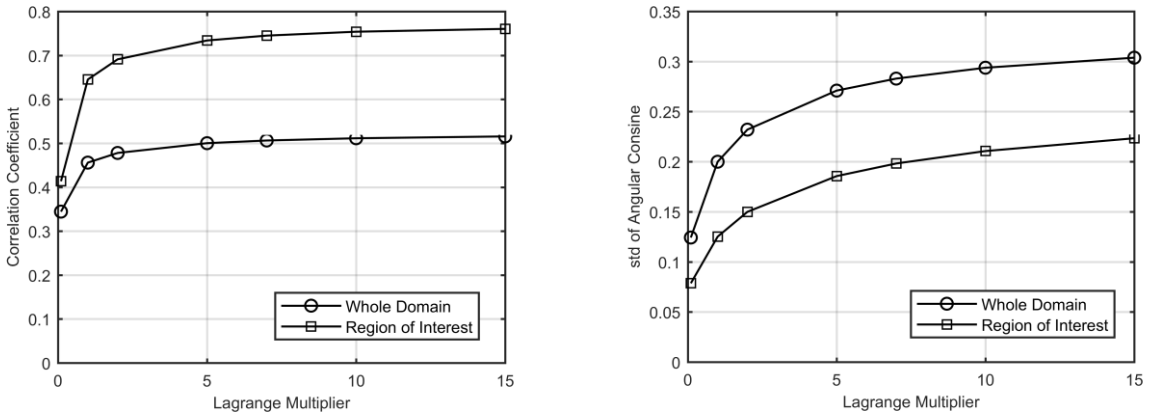

(a) (b)

Figure 8. (a) The correlation coefficient between the magnitudes $|\boldsymbol{u}_\Omega|$ and $|\boldsymbol{\tau}|$, and (b) the std of the angular cosine as a function of the Lagrange multiplier for the maximum displacement of 7 pixels between two consecutive surface enstrophy images.

5. SOF of temperature in NACA 0015 airfoil flow

5.1. TSP measurements

From an experimental point of view, time-resolved TSP measurements using a high-speed camera provide time sequences of surface temperature fields and fluctuation surface temperature energy fields. Therefore, the SOF of temperature $\boldsymbol{u}_T$ can be determined by solving the Euler-Lagrange equation Eq. (31) when the source term f is neglected as a higher-order small term. In complex flows such as separated flows and turbulent flows, the fluctuating surface temperature energy fields usually have spatially intermittent structures associated with near-wall coherent structures, which serve as trackable features in optical flow computation to extract $\boldsymbol{u}_T$. The field of $\boldsymbol{u}_T$ is proportional to the corresponding skin friction field.

To evaluate the feasibility of measuring skin friction by tracking surface temperature features, time-resolved TSP measurements were carried out using a NACA 0015 airfoil in a low-speed wind tunnel with a test section of 0.4 m by 0.4 m at the Applied Aerodynamics Laboratory of Western Michigan University, where the freestream turbulence intensity was about 0.2%. The model had a chord length of 125 mm and a span of 398 mm, which was fully 3D-printed using polylactide. A 130-mm wide spanwise section in the middle of the airfoil was used for TSP measurements. To reduce heat transfer from the heating layer to the model, an insulating rubberized coating was applied as a base layer on the top surface of the model. A uniform surface heating distribution was obtained using a silver-coated copper conductive layer of an approximately 2 mm thickness with the electrical resistivity of 0.00022 Ω-cm (MG Chemical 843AR https://www.mgchemicals.com). Electrical current was applied to the conductive layer using conductive copper tapes as electrodes in the bottom surface near the leading and trailing edges of the model. The electrodes were connected to a 12-V variable amperage power supply in order to produce continuous heating during testing. The upper surface of the heating layer was covered by a white Mylar sheet coated with EuTTA-dope TSP for surface temperature measurements.

The excitation light for the TSP was provided by two UV lights placed on top of the test section of the wind tunnel to ensure approximately uniform illumination. For each test run in a dark environment, a sequence of 100 images (1280×1024 pixels) were acquired using a Chronos 1.4 high-speed camera at 900 fps. A long-pass optical filter (> 550 nm) was amounted on the lens to filter the light captured by the camera allowing only detection of the

luminescent emission of TSP.

The model was tested at the angles of attack (AoAs) of 5° and 10° at a freestream velocity of 15 m/s. The Reynolds number based on the chord length was 1.27×10^5. To visualize surface temperature patterns with TSP, the conductive layer on the model was heated by supplying the power of 480 Watts (12 V and 40 Amps), keeping the heating layer temperature constant at about 30 ºC higher than the freestream temperature before a run. The model surface was maintained continuous heating in the test.

Figure 9 shows the normalized time-averaged surface temperature field ($\langle T_w \rangle / \max(\langle T_w \rangle)$) and surface temperature fluctuation energy field ($\langle e_T \rangle / \max(\langle e_T \rangle)$) on the model at AoA of 5º, which are obtained by averaging 99 instantaneous fields. In Fig. 9 and other relevant figures, *x* is the chordwise coordinate with the origin at the leading edge of the airfoil and *c* is the chord length. The separation bubble near the leading edge is visualized as a region of the higher $\langle T_w \rangle / \max(\langle T_w \rangle)$ and lower $\langle e_T \rangle / \max(\langle e_T \rangle)$ along the spanwise direction. Figure 10 shows the fields of $\langle T_w \rangle / \max(\langle T_w \rangle)$ and $\langle e_T \rangle / \max(\langle e_T \rangle)$ on the model at AoA of 10º. Figures 11 and 12 show the spanwise-averaged profiles of $\langle T_w \rangle / \max(\langle T_w \rangle)$ and $\langle e_T \rangle / \max(\langle e_T \rangle)$ at AoAs of 5º and 10º, respectively. The location of the separation bubble moves toward the leading edge as AoA increases from 5º to 10º. The peaks of $\langle e_T \rangle$ in both the cases occur after flow attachment due to the Görtler-like instability.

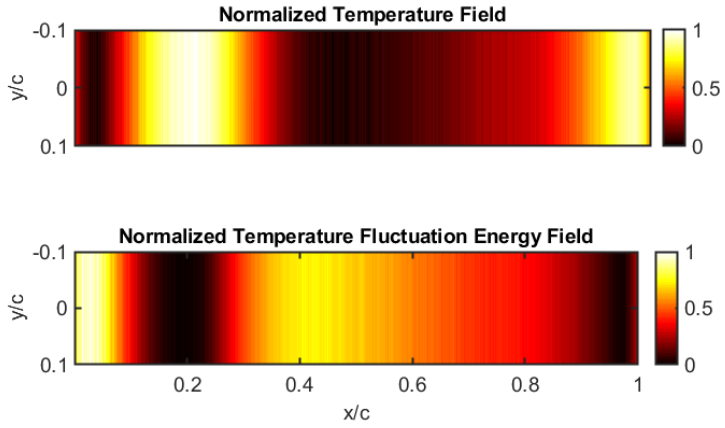

Figure 9. Normalized time-averaged surface temperature field (above), and surface temperature fluctuation energy field (lower) on a NACA 0015 airfoil model at AoA = 5º.

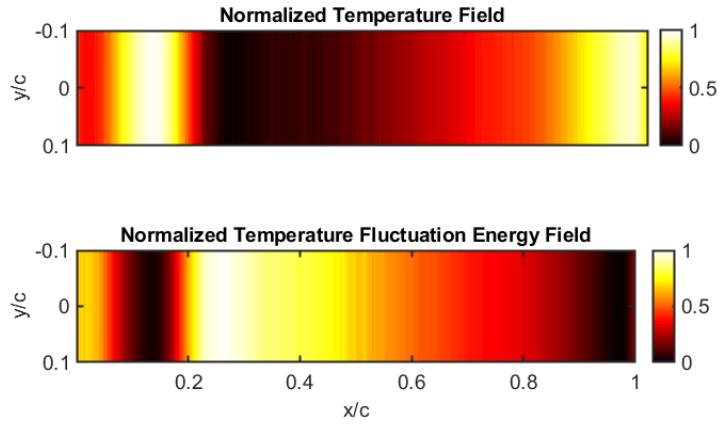

Figure 10. Normalized time-averaged surface temperature field (above), and surface temperature fluctuation energy field (lower) on a NACA 0015 airfoil model at AoA = 10º.

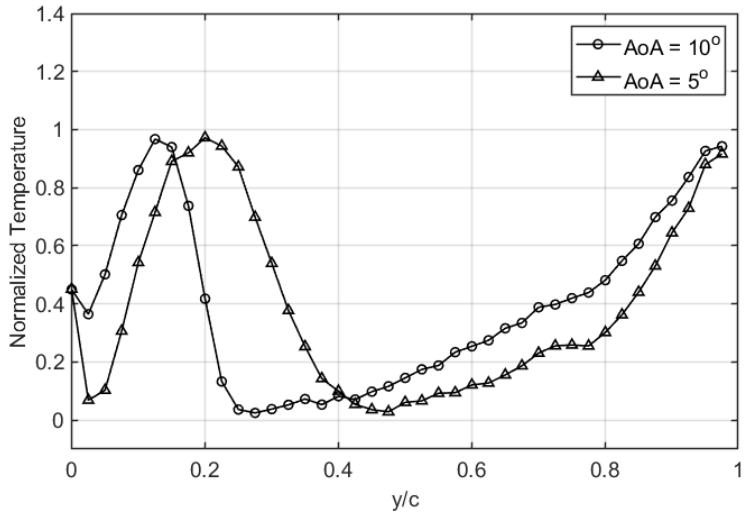

Figure 11. Profiles of the time-averaged surface temperature on a NACA 0015 airfoil model at AoAs of 5° and 10°.

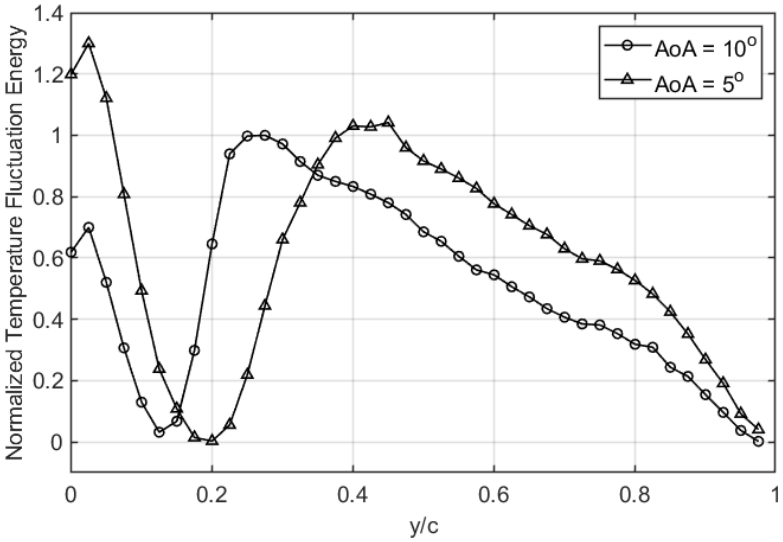

Figure 12. Profiles of the time-averaged surface temperature fluctuation energy on a NACA 0015 airfoil model at AoAs of 5° and 10°.

The SOF of temperature $\boldsymbol{u}_T$ is calculated from a pair of sequential e_T-images, and thus a sequence of $\boldsymbol{u}_T$-fields is obtained. Figure 13 shows the fields of the magnitude and vectors of the SOF on a NACA 0015 airfoil model at AoAs of 5° and 10°. Figures 14 and 15 show

the spanwise-averaged profiles of the normalized streamwise component of the SOF at AoAs of 5° and 10°, respectively. In these figures, the normalized skin friction profiles obtained using the GLOF method are also plotted for comparison. The separation bubble is clearly identified as a region with the negative streamwise skin friction component that is characterized by the separation and attachment lines. As expected, the location of the separation bubble approaches to the leading edge at AoA of 10°. After the flow attachment, the skin friction magnitude rapidly increases and reaches to the maximum at a downstream location (x/c = 0.55 for AoA of 5° and 0.4 for AoA of 10°). The rapid increase of the skin friction magnitude corresponds to that of the time-averaged temperature fluctuation energy shown in Fig. 12. This indicates that the elevated skin friction after the attachment is caused by enhanced turbulence. These profiles of the SOF are consistent with the data obtained by Miozzi et al. [19] using the correlation method and Taylor hypothesis method on a NACA 0015 hydrofoil section in a water tunnel.

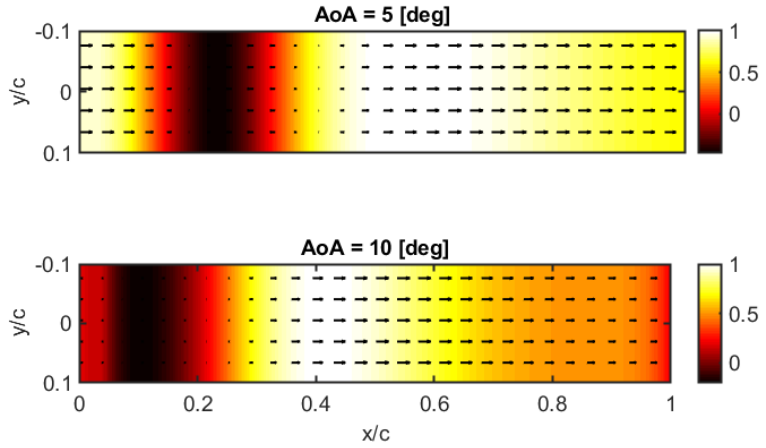

Figure 13. The fields of the magnitude and vectors of the SOF on a NACA 0015 airfoil model at AoAs of 5° and 10°.

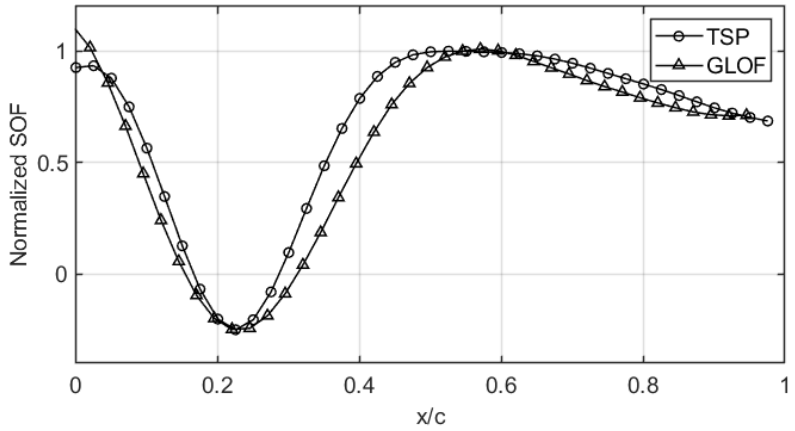

Figure 14. The spanwise-averaged profiles of the normalized streamwise component of the SOF obtained using the optical flow method on a NACA 0015 airfoil model at AoA of 5°. The normalized skin friction profile obtained using the GLOF method is also plotted for comparison.

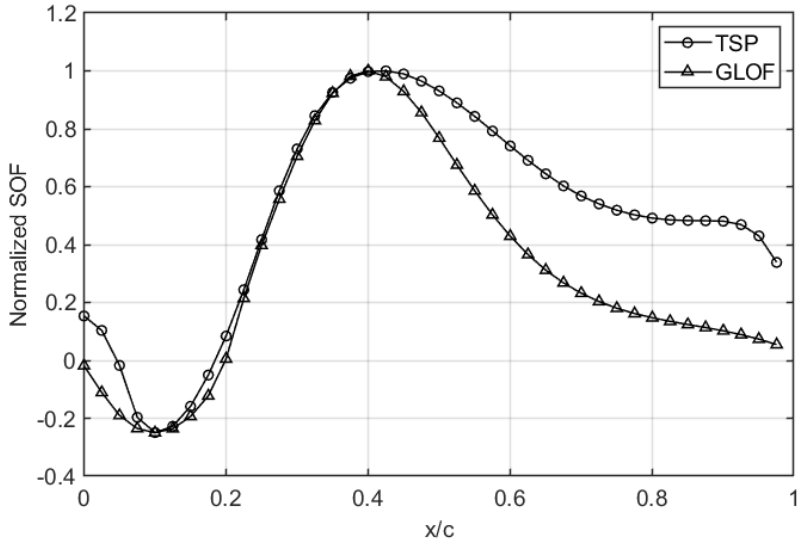

Figure 15. The spanwise-averaged profiles of the normalized streamwise component of the SOF obtained using the optical flow method on a NACA 0015 airfoil model at AoA of 10°. The normalized skin friction profile obtained using the GLOF method is also plotted for comparison.

5.2. GLOF skin friction measurements

To validate the results of the SOF of temperature, global luminescent oil-film (GLOF) skin friction measurements on the same NACA 0015 airfoil model was carried out in the same

flow conditions. The middle section of the models was covered by a white Mylar sheet for enhancing luminescent emission. Luminescent oil was made by blending an oil-based UV dye (Petroleum Tracer Concentrate DFSB-K175 from Risk Reactor, www.riskreactor.com) with polydimethylsiloxane (PDMS, silicone oil) with the viscosity of 200 cs. Luminescent oil was brushed carefully onto a model surface to ensure uniform oil film application. The resulting luminescent oil emitted the radiation at a longer wavelength (about 550-620 nm) when excited by UV illumination. Two UV lamps were positioned to ensure a uniform illumination field in the test section. A long-pass filter (> 550 nm) was used for the detection of the luminescent emission centered at approximately 590 nm. The wind tunnel was run in a dark environment, and images were captured by Basler Aviator CCD camera at 16 fps.

The working principle of the GLOF skin friction meter was described by Liu et al. [39]. For GLOF visualization on a surface, an equation relating the projected skin friction to the normalized luminescent intensity in the image plane was derived from the thin-oil-film equation. Interestingly, this equation has the same mathematical form as the physics-based optical flow equation. Therefore, extraction of skin friction from luminescent oil images can be solved as an optical flow problem using the variational method (similar to the problem described in Section 3). A relative time-averaged skin friction field is reconstructed by averaging a sequence of snapshot solutions of the Euler-Lagrange equations for this inverse problem. The GLOF method has been used to measure skin friction fields in complex separated flows [12, 13, 40]. The skin friction fields were reconstructed by averaging a sequence of snapshot solutions of the Euler-Lagrange equations. Figure 16 shows typical

GLOF images on a NACA 0015 airfoil model at AoAs of 5º and 10º. Figure 17 shows the normalized skin friction fields extracted by the GLOF method. The normalized spanwise averaged profiles of the streamwise skin friction component are plotted in Figs. 14 and 15 for comparison with those of the normalized streamwise component of the SOF. The results of the SOF and skin friction are consistent.

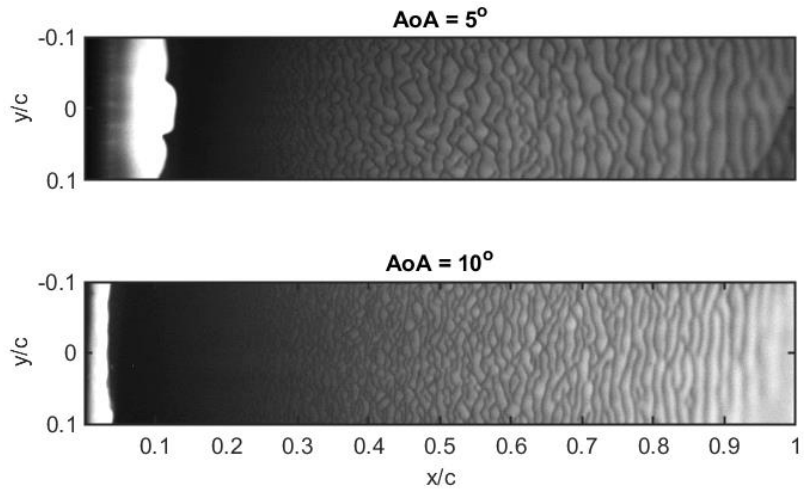

Figure 16. Typical GLOF images on a NACA 0015 airfoil model at AoAs of 5º and 10º. The freestream flow is from left to right.

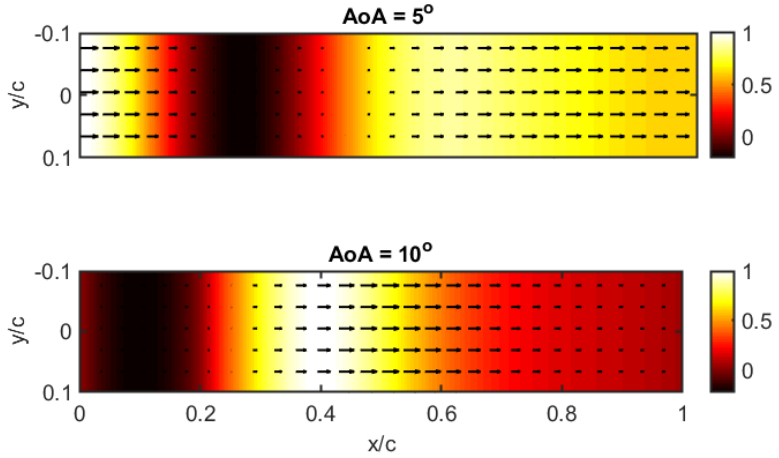

Figure 17. Normalized skin friction magnitude fields and vectors obtained by using the GLOF method on a NACA 0015 airfoil model at AoAs of 5º. and 10º.

6. SOF of temperature in an impinging jet

The field of the SOF of temperature was determined from TSP measurements in an impinging jet. The low-speed air jet facility was similar to that used by Liu and Sullivan [42]. The impinging jet experimental setup consisted of a primary rectangular settling chamber (203 mm ×304 mm × 304 mm) connected to a secondary 147 mm long cylindrical chamber with a 50.8 mm diameter. A contoured nozzle with an exit diameter (D) of 2 mm, a length of 35 mm and a contraction ratio of 5.6 was placed at the end of the cylindrical chamber. Using compressed air introduced in the primary settling chamber, the nozzle was able to produce an air jet flow. The exit jet velocity was set at $U_o = 50\ m/s$, and the corresponding Reynolds number was $Re_D = U_o D/\nu = 6.2\times10^3$. The ratio between the nozzle-to-surface distance and the nozzle diameter was $H/D = 6$. The impingement angle was variable, which was defined as the angle between axisymmetric axis and the impingement surface.

To measure surface temperature, the jet impinged on a 177.8 mm wide, 228.6 mm long and 0.0254 mm thick stainless-steel sheet heated electrically. Two aluminum rods with diameters of 38.1 mm where used as electrodes. The sheet was held in place using four tension coil springs (two in each side). The stainless-steel sheet was heated to a surface temperature of 70 °C by supplying the total power of 600 watts (50 A and 12 V) across the sheet using a power generator. EuTTA-dope TSP was used in the experiments and the calibration curve for this TSP was described by Liu et al. [43]. A 10 μm thick TSP layer was applied using an airbrush on a white Mylar film on the backside of the sheet. During testing,

the TSP was excited using two UV lamps. TSP images were acquired using a 12-bit Chronos 1.4 high-speed camera at a frame rate of 480 fps (frames per second) with a resolution of 730×570 pixels. The camera was equipped with a long-pass optical filter (>570 nm).

Figure 18(a) shows a time-averaged field of the surface temperature difference ($\langle T_w - T_{ref} \rangle$) on the impingement surface when the impingement angle is 90° (normal impingement), where T_{ref} is the ambient temperature. Figure 18(b) shows a normalized time-averaged field of the surface temperature fluctuation energy ($\langle e_T \rangle / \max(\langle e_T \rangle)$). The SOF of temperature is calculated from a pair of sequential e_T-images with a time interval of 10 ms between them, and thus a sequence of $\boldsymbol{u}_T$-fields is obtained. Figure 18(c) shows the time-averaged $\boldsymbol{u}_T$-field over 100 snapshot fields and the $\boldsymbol{u}_T$-magnitude field normalized by its maximum value of the ring structure. Figure 19 shows the transverse profile of the time-averaged SOF magnitude normalized the maximum value of skin friction in comparison with the hot-film skin friction data obtained by Liu and Woodiga [15] in a normally impinging jet from a circular tube in the similar conditions. The profile of the SOF and hot-film skin friction data are consistent particularly in the impingement region. Figure 20 shows the normalized skin friction vectors and magnitude fields in the impinging jet at the impingement angles of 75°, 45°, and 30°. The skin friction distribution becomes more asymmetrical relative to the *x*-axis (the transverse axis across the impingement point) as the impingement angle decreases.

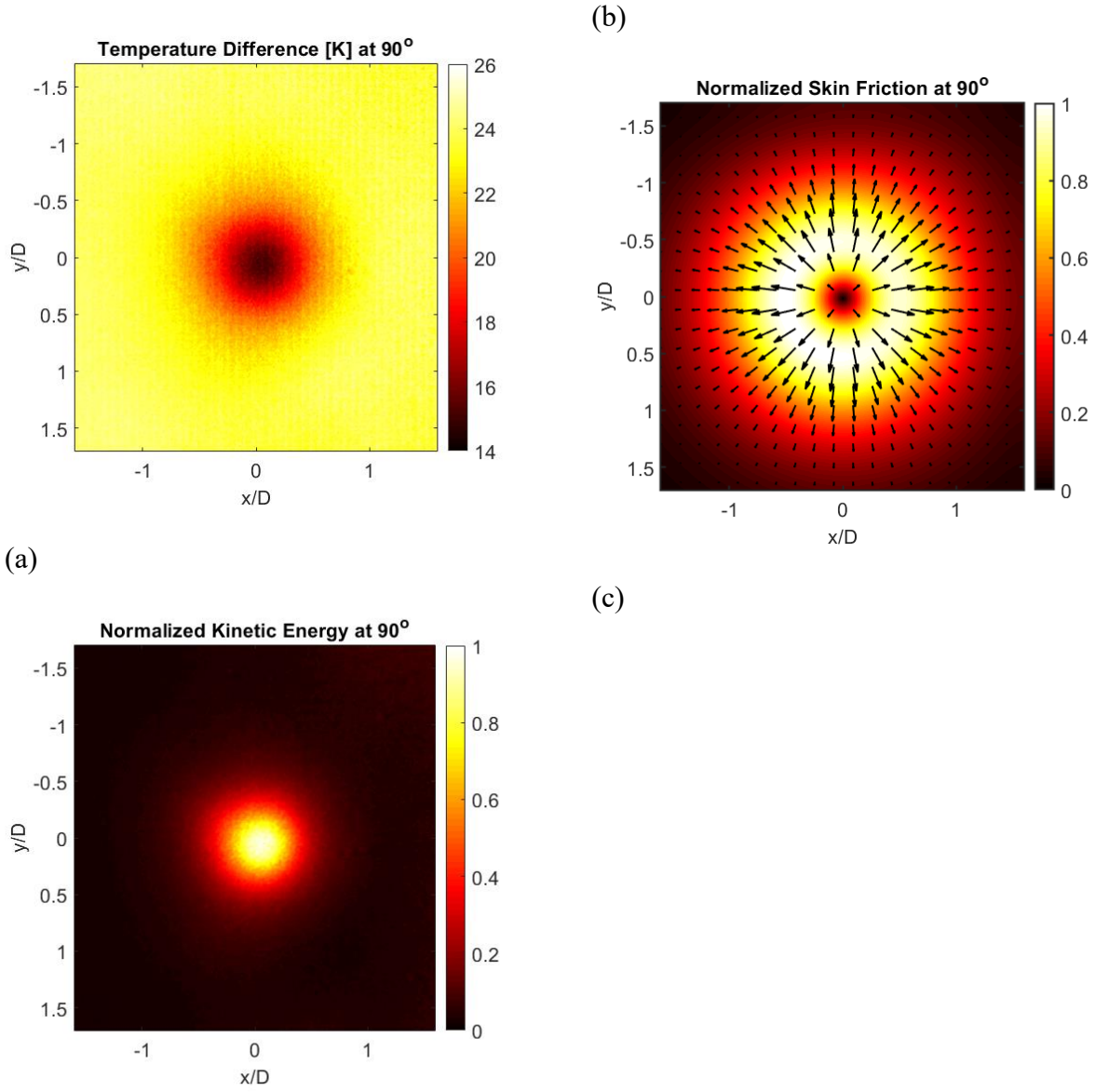

Figure 18. Time-averaged fields in a normally impinging jet: (a) surface temperature difference, (b) normalized surface temperature fluctuation kinetic energy, and (c) normalized skin friction vectors and magnitude.

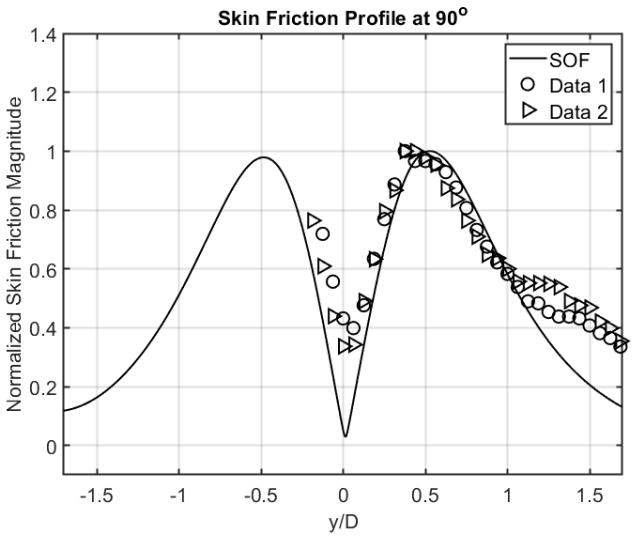

Figure 19. Profile of the normalized SOF magnitude in comparison with the hot-film data in the normally impinging jet.

(b)

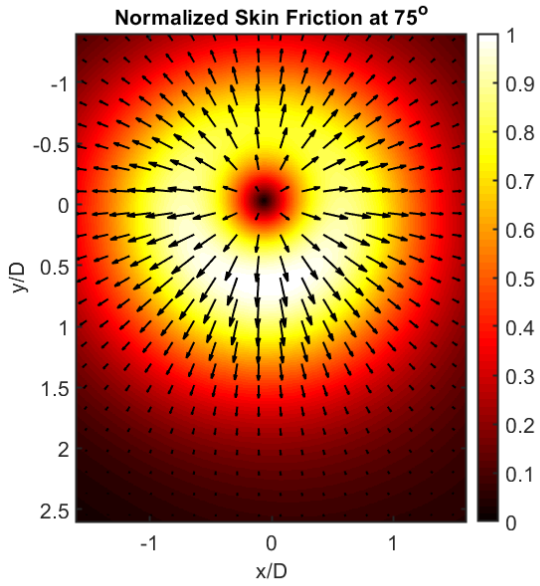

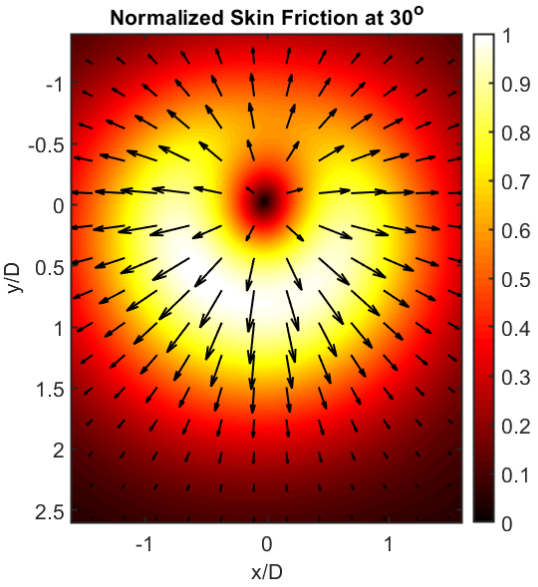

(a)

(c)

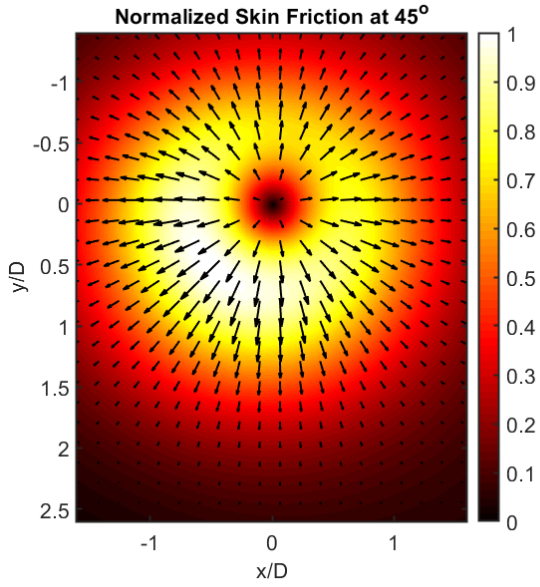

Figure 20. Normalized skin friction vectors and magnitude fields in the impinging jet at different impingement angles: (a) 75º, (b) 45º, and (c) 30º.

7. Conclusions

The evolution equations of surface temperature, relative concentration and enstrophy are given to elucidate the relationship between the surface optical flow (SOF) and skin friction in viscous flows. The SOF is defined as the convection velocity of a specific surface quantity (temperature, scalar, or enstrophy), which is proportional to skin friction when some smaller terms are neglected in the first-order approximation. The evolution equations of surface temperature, scalar and enstrophy are written as a generic form of the optical flow equation. Therefore, the SOF can be determined by solving the optical flow problem from a time sequence of fields of a surface quantity (temperature, scalar concentration, or enstrophy). This method is useful to extract a skin friction field from surface flow visualizations particularly temperature sensitive paint (TSP) measurements. In the first example, this method is applied to instantaneous surface enstrophy fields obtained by direct numerical simulation (DNS) of a turbulent channel flow. The fields of the SOF of the enstrophy extracted using the optical flow method are highly correlated with the corresponding skin friction fields, validating the theoretical analysis based on the evolution equation of the surface enstrophy. Further, time-resolved TSP measurements on a NACA 0015 airfoil model in a wind tunnel were conducted to examine the proposed optical flow method. The time- and spanwise-averaged profiles of the SOF of temperature show the separation bubble near the leading edge on the upper surface of the model at the angles of attack of 5^{o} and 10^{o}. The SOF results obtained using the optical flow method are consistent with those obtained by global luminescent oil-film (GLOF) skin friction measurements. In addition, time-resolved TSP

measurements on an impinging jet were conducted at different impingement angles. The time-averaged SOF magnitude distribution in the normally impinging jet is in good agreement with the skin friction data obtained using a hot-film senor in the similar flow conditions.

Appendix: Note on surface enstrophy convection velocity

The transport equation of the enstrophy is

$$\frac{\partial \Omega}{\partial t} + \boldsymbol{u} \cdot \tilde{\nabla} \Omega = \boldsymbol{\omega} \cdot \boldsymbol{S} \cdot \boldsymbol{\omega} + \nu \tilde{\nabla}^2 \Omega - \nu \tilde{\nabla} \boldsymbol{\omega} : \tilde{\nabla} \boldsymbol{\omega}, \tag{A1}$$

where $\Omega = |\boldsymbol{\omega}|^2 / 2$ is the enstrophy,, $\boldsymbol{\omega}$ is the vorticity, $\boldsymbol{u}$ is the velocity, $\boldsymbol{S}$ is the strain rate tensor, ν is the kinematic viscosity, and $\tilde{\nabla} = \partial / \partial x_k$ ($k = 1,2,3$) is the gradient operator in a 3D space. By applying the Caswell-Wu formula to the vortex stretching term on a stationary surface [41]

$$\boldsymbol{\omega}_w \cdot \boldsymbol{S}_w \cdot \boldsymbol{\omega}_w = \frac{1}{2} \boldsymbol{\omega}_w \cdot \left[\boldsymbol{n} \left(\boldsymbol{\omega}_w \times \boldsymbol{n} \right) + \left(\boldsymbol{\omega}_w \times \boldsymbol{n} \right) \boldsymbol{n} \right] \cdot \boldsymbol{\omega}_w = 0,$$

Eq. (A1) is reduced to

$$\frac{\partial \Omega_w}{\partial t} + \left[\nu \tilde{\nabla} \boldsymbol{\omega} : \tilde{\nabla} \boldsymbol{\omega} \right]_w - \nu \left[\frac{\partial^2 \Omega}{\partial x_3^2} \right]_w = \nu \nabla^2 \Omega_w, \tag{A2}$$

where $\nabla = \partial / \partial x_i$ ($i = 1,2$) is the gradient operator on a surface. Comparison of Eq. (A2) with Eq. (22) yields

$$\boldsymbol{u}_\Omega \cdot \nabla \Omega_w = \left[\nu \nabla \boldsymbol{\omega} : \nabla \boldsymbol{\omega} \right]_w - \nu \left[\frac{\partial^2 \Omega}{\partial x_3^2} \right]_w. \tag{A3}$$

According to Eq. (A3), the convection term $\boldsymbol{u}_\Omega \cdot \nabla \Omega_w$ is approximately dominated by the viscous dissipation term on a wall, which is positive physically, when $\nu \left[\partial^2 \Omega / \partial x_3^2 \right]_w$ is sufficiently small. Further, the dissipation term can be decomposed, i.e.,

$$\begin{aligned}\left[\nu\tilde{\nabla}\boldsymbol{\omega}:\tilde{\nabla}\boldsymbol{\omega}\right]_w &= \nu\left(\nabla\boldsymbol{\omega}_w+\boldsymbol{n}\left[\frac{\partial\boldsymbol{\omega}}{\partial x_3}\right]_w\right):\left(\nabla\boldsymbol{\omega}_w+\boldsymbol{n}\left[\frac{\partial\boldsymbol{\omega}}{\partial x_3}\right]_w\right)\\ &= \nu\nabla\boldsymbol{\omega}_w:\nabla\boldsymbol{\omega}_w+\nu\left[\frac{\partial\boldsymbol{\omega}}{\partial x_3}\right]_w\cdot\left[\frac{\partial\boldsymbol{\omega}}{\partial x_3}\right]_w\end{aligned}. \tag{A4}$$

According to Wu et al. [41], since the wall-normal derivative of $\boldsymbol{\omega}$ at a wall is expressed as

$$\left[\frac{\partial\boldsymbol{\omega}}{\partial x_3}\right]_w = \mu^{-1}\boldsymbol{n}\times\nabla p_w-\left(\nabla\cdot\boldsymbol{\omega}_w\right)\boldsymbol{n}, \tag{A5}$$

we have

$$\left[\nu\tilde{\nabla}\boldsymbol{\omega}:\tilde{\nabla}\boldsymbol{\omega}\right]_w = \nu\nabla\boldsymbol{\omega}_w:\nabla\boldsymbol{\omega}_w+\rho^{-2}\nu^{-1}\left|\nabla p_w\right|^2+\nu\left|\nabla\cdot\boldsymbol{\omega}_w\right|^2. \tag{A6}$$

Therefore, the convection term is expressed as

$$\boldsymbol{u}_\Omega\cdot\nabla\Omega_w = S_\Omega, \tag{A7}$$

where

$$S_\Omega = \nu\nabla\boldsymbol{\omega}_w:\nabla\boldsymbol{\omega}_w+\frac{1}{\rho^2\nu}\left|\nabla p_w\right|^2+\nu\left|\nabla\cdot\boldsymbol{\omega}_w\right|^2-\nu\left[\frac{\partial^2\Omega}{\partial x_3^2}\right]_w. \tag{A8}$$

Acknowledgements:

T. Liu and D. Salazar were supported by the NASA SBIR Phase 2 (7032840). In addition, T. Liu is partially supported by the Presidential Innovation Professorship at Western Michigan University.

Data Availability:

The data that support the findings of this study are available from the corresponding author upon reasonable request.

References:

[1] J. C. R. Hunt, C. J. Abell, J. A. Peterka. and H. Woo, "Kinematical studies of the flows around free or surface-mounted obstacles; applying topology to flow visualization," J. Fluid Mech. **88**, 179-200 (1978).

[2] M. Tobak and D. J. Peake, "Topology of three-dimensional separation flows," Annu. Rev. Fluid Mech. **14**, 61-85 (1982).

[3] A. E. Perry and M. S. Chong, "A series-expansion study of the Navier-Stokes equations with applications to three-dimensional separation patterns," J. Fluid Mech. **173**(11), 207-223 (1986).

[4] J. Z. Wu, R. W. Tramel. F. L. Zhu and X. Y. Yin, "A vorticity dynamics theory of three-dimensional flow separation," Phys. Fluids **12**, 1932-1954 (2000).

[5] J. M. Délery, "Robert Legendre and Henri Werle: Toward the elucidation of three-dimensional separation," Annu. Rev. Fluid Mech. **33**, 129-154 (2001).

[6] E. H. Hirschel, J. Cousteix and W. Kordulla, "Three-dimensional attached viscous flows," Springer, Berlin, Chapter 7 (2014).

[7] A. E. Perry and M. S. Chong, "A description of eddying motions and flow patterns using critical-point concepts," Annu. Rev. Fluid Mech. **19**, 125-55 (1987).

[8] T. Bewley and B. Protas, "Skin friction and pressure: the "footprints" of turbulence." Physica D **196**(1-2), 28-44 (2004).

[6] A. Surana, O. Grunberg and G. Haller, "Exact theory of three-dimensional flow separation. Part 1. Steady separation," J. Fluid Mech. **564**, 57-103 (2006).

[10] T. Liu, “Skin-friction and surface-pressure structures in near-wall flows,” AIAA J. **56**(10), 3887-3896 (2018).

[11] T. Chen, T. Liu, L.-P. Wang, and S. Chen, “Near-wall flow structures and related surface quantities in wall-bounded turbulence,” Phys. Fluids **33**, 065116 (2021).

[12] T. Liu, “Extraction of skin-friction fields from surface flow visualizations as an inverse problem,” Meas. Sci. Technol. **24**, 124004 (2013).

[13] T. Liu, “Global skin friction measurements and interpretation,” Prog. Aero. Sci. **111**, 100584 (2019).

[14] T. Chen, T. Liu, L.-P. Wang, and S. Chen, “Relations between skin friction and other surface quantities in viscous flows,” Phys. Fluids **31**, 107101 (2019).

[15] T. Liu and S. Woodiga, “Feasibility of global skin friction diagnostics using temperature sensitive paint,” Meas. Sci. Technol. **22**, 115402 (2011).

[16] M. Miozzi, A. Capone, F. Di Felice, C. Klein and T. Liu. “Global and local skin friction diagnostics from TSP surface patterns on an underwater cylinder in cross flow,” Phys. Fluids **28**, 12410 (2016).

[17] M. Miozzi, A. Capone, M. Costantini, L. Fratto, C. Klein, and F. Di Felice, “Skin friction and coherent structures within a laminar separation bubble,” Exp. Fluids **60**, 1–25 (2019).

[18] M. Miozzi, A. Capone, C. Klein and M. Costantini, “Incipient stall characterization from skin-friction maps,” Int. J. Numer. Methods Heat Fluid Flow **31** 674–93 (2020).

[19] M. Miozzi, F. Di Felice, C. Klein and M. Costantini, “Taylor hypothesis applied to direct measurement of skin friction using data from temperature sensitive paint,” Exp. Therm.

Fluid Sci. **110**, 109913 (2020).

[20] M. Miozzi1 and M. Costantini, “Temperature and skin-friction maps on a lifting hydrofoil in a propeller wake,” Meas. Sci. Technol. **32**, 114007 (2021).

[21] H. Eckelmann, “The structure of the viscous sublayer and the adjacent wall region in a turbulent channel flow,” J. Fluid Mech. **65**(3), 439–459 (1974).

[22] J. Kim and F. Hussain, “Propagation velocity of perturbations in turbulent channel flow,” Phys. Fluids A **5**, 695 (1993)

[23] J. C. Del Álamo, J. Jiménez, “Estimation of turbulent convection velocities and corrections to Taylor’s approximation,” J. Fluid Mech. **640**, 5–26 (2009).

[24] C. Geng, G. He, Y. Wang, C. Xu, A. Lozano-Durán, J. M. Wallace, “Taylor’s hypothesis in turbulent channel flow considered using a transport equation analysis,” Phys. Fluids **27**(2) 025111 (2015).

[25] G. P. Romano, “Analysis of two-point velocity measurements in near-wall flows,” Exp. Fluids **20**(2) 68–83 (1995).

[26] B. C. Khoo, Y. T. Chew, and C. J. Teo, “Near-wall hot-wire measurements. Part II: turbulence time scale, convective velocity and spectra in the viscous sublayer,” Exp. Fluids **31**(5), 494–505 (2001).

[27] C. Atkinson, N. A. Buchmann, and J. Soria, “An experimental investigation of turbulent convection velocities in a turbulent boundary layer,” Flow, Turbul. Combust. **94**(1), 79–95 (2015).

[28] G. Hetsroni, I. Tiselj, R. Bergant, A. Mosyak, and E. Pogrebnyak, “Convection velocity

of temperature fluctuations in a turbulent flume," J. Heat Transf. **126**(5), 843–848 (2004).

[29] T. Liu, S. Woodiga, J. Gregory and J. Sullivan, "Global skin friction diagnostics based on surface mass-transfer visualizations," AIAA J. **52**, 2369-2383 (2014).

[30] T. Liu, M. H. Makhmalbaf, R. S. V. Ramasamy, S. Kode and P. Merati, "Skin friction fields and surface dye patterns on delta wings in water flows," J. Fluids Eng. **137**, 071202 (2015).

[31] T. Chen, T. Liu, L.-P. Wang, and S. Chen, "Features of surface physical quantities and temporal-spatial evolution of wall-normal enstrophy flux in wall-bounded flows," Phys. Fluids (accepted) (2021).

[32] B. K. Horn and B. G Schunck, "Determining optical flow," Artificial Intelligence **17**(1-3), 185-204 (1981).

[33] T. Liu. and L. Shen. "Fluid flow and optical flow," J. Fluid Mech. **614**, 253-291 (2008).

[34] G. Aubert and P. Kornprobst, "A mathematical study of the relaxed optical flow problem in the space $BV(\Omega)$," SIAM J. Math. Anal. **30**,1282-1308 (1999).

[35] G. Aubert, R. Deriche and P. Kornprobst, "Computing optical flow via variational techniques," SIAM J Appl Math **60**,156-182 (1999).

[36] B. Wang, Z. Cai, L. Shen, and T. Liu, "An analysis of physics-based optical flow method," J. Comp. Appl. Math. **276**, 62-80 (2015).

[37] A. N. Tikhonov and V. Y. Arsenin., "Solutions of ill-posed problems," Wiley, New York, Chapter II (1977).

[38] C. W. Groetsch, "Inverse problems in the mathematical sciences," Vieweg Braunschweig, Chapter 5 (1993).

[39] T. Liu, J. Montefort, S. Woodiga, P. Merati, and L. Shen, “Global luminescent oil film skin friction meter,” AIAA J. **46**(2):476-485 (2008).

[40] T. Liu “Extraction of skin-friction fields from surface flow visualizations as an inverse problem,” Meas. Sci. Technol. **24**, 124004 (2013).

[41] J.-Z. Wu, Y.-T. Yang, Y.-B. Luo and C. Pozrikidis, “Fluid kinematics on a deformable surface,” J. Fluid Mech. **541**, 371-381 (2005,).

[42] T. Liu and J. Sullivan, “Heat transfer and flow structures in an excited circular impinging jet,” Int. J. Heat Mass Transf. **39**, 3695-3706 (1996).

[43] T. Liu, J. P. Sullivan, K. Asai, C. Klein, and Y, Egami, “Pressure and temperature sensitive paints (Second Edition),” Springer, Berlin (2021).